Environmental Science Advances

ROYAL SOCIETY OF CHEMISTRY

PAPER

View Article Online
View Journal | View Issue

Check for updates

Cite this: *Environ. Sci.: Adv.*, 2025, **4**, 1488

Improving photocatalytic efficiency through Cu substitution in TiO_2/g-C_3N_4 heterojunction nanocomposites for wastewater remediation†

Phyu Phyu Cho,[a] Phyu Phyu Mon,[a] Mohit Kumar,[ab] Saiyam Dobhal[a] and Subrahmanyam Challapalli *[a]

Received 27th March 2025
Accepted 30th June 2025

DOI: 10.1039/d5va00080g

rsc.li/esadvances

Water pollution from organic contaminants is one of the biggest problems affecting the globe today. Conventional wastewater treatment systems have been used many times to solve world water pollution problems. This study focuses on the development of Cu doped TiO_2/g-C_3N_4 heterojunction nanocomposites to improve the effectiveness of visible light harvesting, increase charge separation and transfer efficiency, and enhance photocatalytic activity for the degradation of organic contaminants. The synthesized photocatalysts were extensively analysed using XRD, FTIR, BET, UV DRS, PL, SEM, TEM, and XPS methodologies. The superior photocatalyst (Cu-TiO_2/g-C_3N_4) achieved the highest photocatalytic degradation efficiency for BPA, MB, CR, and EBT under visible light irradiation. The rate constant for photocatalytic degradation of BPA over the Cu-TiO_2/g-C_3N_4 photocatalyst was 10.83, 8.86 and 3.48 fold greater than that of pure TiO_2, pristine g-C_3N_4, and Cu-TiO_2 photocatalysts, respectively. The rate constant decreased with the introduction of AO and TBA as they scavenge holes and hydroxyl radicals, respectively. The increased photocatalytic activity of the ternary photocatalyst is attributed to improved electron–hole pair separation and the creation of the type-II heterojunction structure. The photocatalytic parameters of BPA demonstrate that the Cu-TiO_2/g-C_3N_4 photocatalyst could be used in real-world wastewater treatment applications.

Environmental significance

Clean water is essential for life, and many water sources are increasingly contaminated by hazardous organic chemicals. Traditional treatment methods often fall short in effectively removing these persistent pollutants. This work highlights the environmental promise of a Cu-doped TiO_2/g-C_3N_4 nanocomposite, which acts as a solar-activated catalyst to break down harmful compounds in water. Its innovative design promotes strong visible light absorption and efficient charge separation, enabling faster degradation of pollutants. By using sunlight as the driving force, this photocatalyst offers a green and cost-effective alternative for water purification. The approach aligns with global efforts to develop sustainable technologies for environmental cleanup and demonstrates real potential for practical application in wastewater treatment systems.

1 Introduction

Currently, pollution and the global energy crisis are major concerns for animals, plants, and humans.[1] Water contamination has increased due to highly toxic heavy metals such as chromium (Cr VI) and numerous organic pollutants including methylene blue (MB), Congo red (CR), eriochrome black T (EBT), and phenols, among others, as a result of population growth and industrialization.[2–5] The aforementioned organic contaminants react with air and water, producing harmful end products. Thus, it is critical to easily degrade water pollutants.[6] To support sustainable development, several technologies have been developed to treat organic contaminants in water, including microbial degradation, activated carbon adsorption, electrochemical coagulation, filtration, and photocatalysis.[7]

Photocatalytic technology has several uses, but one of the most important is the removal of pollutants from wastewater. It is very efficient, does not produce any secondary pollutants, and can transform solar energy into chemical energy under mild conditions. Many semiconductor materials, including metal oxides, metal sulfides, and composites, have been studied for photocatalytic degradation.[8] Among these, titanium dioxide (TiO_2) has attracted a lot of attention because of various advantages including low cost, nontoxicity, and great photocatalytic activity. The photocatalytic activity of TiO_2, a typical wide gap semiconductor with an energy gap of 3.2 eV, is limited by its

[a]*Department of Chemistry, Indian Institute of Technology Hyderabad, Kandi, Sangareddy, 502285, Telangana, India. E-mail: csubbu@iith.ac.in*

[b]*Department of Chemistry and Biochemistry, School of Science Computing and Engineering, Swinburne University of Technology, Hawthorn, VIC, 3122, Australia*

† Electronic supplementary information (ESI) available. See DOI: https://doi.org/10.1039/d5va00080g

Open Access Article. Published on 17 July 2025. Downloaded on 1/22/2026 11:30:53 AM. This article is licensed under a Creative Commons Attribution 3.0 Unported Licence.

© 2025 The Author(s). Published by the Royal Society of Chemistry

Open Access Article. Published on 17 July 2025. Downloaded on 1/22/2026 11:30:53 AM. This article is licensed under a Creative Commons Attribution 3.0 Unported Licence.

intrinsic narrow light-absorption range and high recombination possibility of photogenerated electron–hole pairs.[9] Hence, elemental doping, morphological modification using nanotubes and fibers, and synthesising composites using novel 2-D materials such as graphene and C_3N_4 are effective methods to address these constraints. Elemental doping effectively adjusts the band gap of TiO_2 by creating new energy levels and altering the conduction and valence band minima. Cu-doped TiO_2 has been tested for photocatalytic applications, including hydrogen production, CO_2 conversion, and degradation of dyes and organic pollutants.[10] Woo Kim *et al.* reported Cu existing in Cu-doped TiO_2 thin films in both Cu^+ and Cu^{2+} forms. Under visible light, these nano-architectures displayed better activity for breakdown of organic dye molecules.[11] TiO_2 has therefore been combined with other semiconductors to generate type I and type II heterojunctions in order to improve charge separation.[12,13]

Metal-free semiconductor g-C_3N_4 is often produced using precursors such as urea, melamine, cyanamide, *etc.* Its structural monomers are either tri-*s*-triazine or *s*-triazine units, or the sheets have a honeycomb-like structure. g-C_3N_4 has been coupled with other materials including TiO_2,[14] ZnO,[15] Fe_2O_3,[16] SnO_2,[17] V_2O_5,[18] Bi_2O_4,[19] α-MoC_{1-x} quantum dots,[20] charcoal[21] *etc.* Using g-C_3N_4 alone often leads to fast recombination of electron–hole pairs, which limits its photocatalytic efficiency. Enhancing charge separation is thus crucial for improving its performance. Liyanaarachchi *et al.* reported that Cu-doped TiO_2 was coupled with g-C_3N_4 to form a Z-scheme heterojunction, and its photocatalytic activity was evaluated for methylene blue degradation using persulfate activation.[22] Huang *et al.* studied TiO_2/g-C_3N_4 heterojunctions with different TiO_2 phases, analysing their properties, sunlight-driven naphthalene degradation, and charge migration using DFT calculations to explore their electronic structures.[23] Md Fauzi *et al.* fabricated a TiO_2/g-C_3N_4 photocatalyst *via* hydrolysis using more $TiCl_4$ than previous studies. The heterojunction showed high UV-driven degradation of dyes, phenol, and caffeine, offering a simple, effective method for pollutant removal.[24] Li *et al.* recovered anatase-phase TiO_2 from spent SCR catalysts *via* alkali leaching and used it to synthesize TiO_2/g-C_3N_4 photocatalysts. Characterized by various techniques, the composite showed efficient RhB degradation under visible light.[25] Hazaraimi *et al.* prepared N-TiO_2/g-C_3N_4 *via* two-step calcination using TiO_2 and melamine, achieving nitrogen doping and g-C_3N_4 exfoliation, which enhanced visible light-driven BPA degradation with a simple, low-cost, and efficient method.[26] Miri *et al.* synthesized TiO_2/g-C_3N_4 *via* a solvothermal method, achieving efficient 4-bromophenol degradation under visible light due to enhanced electron transfer, confirmed by XPS, DRS, PL, and degradation pathway analyses.[27] Alqarni *et al.* synthesized MgO-TiO_2@g-C_3N_4 nanocomposites, demonstrating enhanced photocatalytic degradation of high-concentration organic pollutants *via* a direct S-scheme mechanism under visible light, offering an effective dye decolorization method.[28] Zhang *et al.* developed (A–R)TiO_2/g-C_3N_4 photocatalysts *via* impregnation-calcination using $TiCl_4$ and melamine, achieving porous structures and enhanced TC-HCl degradation, with mechanisms studied through structural, optical, and electrochemical analyses.[29] Eskandari *et al.* synthesized a visible-light-responsive L-arginine-TiO_2/g-C_3N_4 photocatalyst for MNZ and OTC degradation, optimized *via* RSM and CCD, with performance confirmed by XRD, PL, DRS, and radical trapping, showing excellent stability and reusability.[30] Mohamed Isa *et al.* developed TiO_2/GCN nanocomposites using biopolymer pullulan for paracetamol photodegradation, addressing limited studies in drug removal. The impact of GCN loading on structural and photocatalytic performance was thoroughly evaluated.[31] Karthik *et al.* synthesized g-C_3N_4/N-TiO_2 nanocomposites *via* ethanol dispersion and showed enhanced sunlight-driven methylene blue degradation. Photocatalytic efficiency, pH, dye concentration, and catalyst recyclability were systematically studied.[32] Hemmati-Eslamu *et al.* synthesized R-GCN/Cu_3BiS_3 nanocomposites, with the 30% Cu_3BiS_3 sample showing excellent visible-light photocatalytic degradation of TC, AMX, RhB, MO, and Cr(VI), highlighting its promise for wastewater treatment.[33] The lack of recent studies on g-C_3N_4/TiO_2 based nanocomposite photocatalysts for wastewater treatment highlights a research gap, inspiring future work to explore their effectiveness in environmental cleanup applications. Comprehensive studies on the photodegradation of bisphenol A (BPA), methylene blue (MB), Congo red (CR), and eriochrome black T (EBT) using metal-doped TiO_2 combined with g-C_3N_4 are still limited, revealing a notable gap in current photocatalytic research. Metal-doped TiO_2 materials have a narrower energy band gap and are effective in the visible spectrum. However, they have limited photocatalytic activity because of electron–hole pair recombination. Similarly, g-C_3N_4 also displays this drawback. Consequently, the coupling of these two semiconductors would be advantageous, as both semiconductors are visible active. Cu doped TiO_2 was coupled with g-C_3N_4 to produce a type-II heterojunction to evaluate the photocatalytic activity of the synthesized nanocomposite in the photodegradation of organic pollutants (BPA, MB, CR, and EBT). Several factors for the photodegradation including the initial BPA concentration, catalyst dosage, and the pH effect, and trapping study for scavengers was performed. Cu-TiO_2/g-C_3N_4 exhibits enhanced photostability and can be recycled up to 5 times without any reduction in photoactivity or mineralization efficiency. In addition, the type-II heterojunction mechanism for BPA degradation is proposed based on radical production and Mott–Schottky experiments.

2 Experimental

2.1. Materials

Titanium isopropoxide (Alfa Aesar), nitric acid (Merck), 2-propanal (Merck), ethanol (Merck), acetic acid (Merck), copper acetate dihydrate (Sigma-Aldrich), bisphenol A (Alfa Aesar), and eriochrome black (Avra) were used. All the chemicals were used as they are without further purification. Distilled water was used for all the experiments. The synthesis of Cu-TiO_2, g-C_3N_4, and Cu-TiO_2/g-C_3N_4 nanocomposites is presented in Fig. 1.

2.2. Preparation of photocatalytic materials (Cu-TiO_2, g-C_3N_4, and Cu-TiO_2/g-C_3N_4)

Pure TiO_2 and Cu-doped TiO_2 were synthesized by using the sol–gel method. For TiO_2 synthesis, 3.3 mL of titanium

Open Access Article. Published on 17 July 2025. Downloaded on 1/22/2026 11:30:53 AM.
This article is licensed under a Creative Commons Attribution 3.0 Unported Licence.

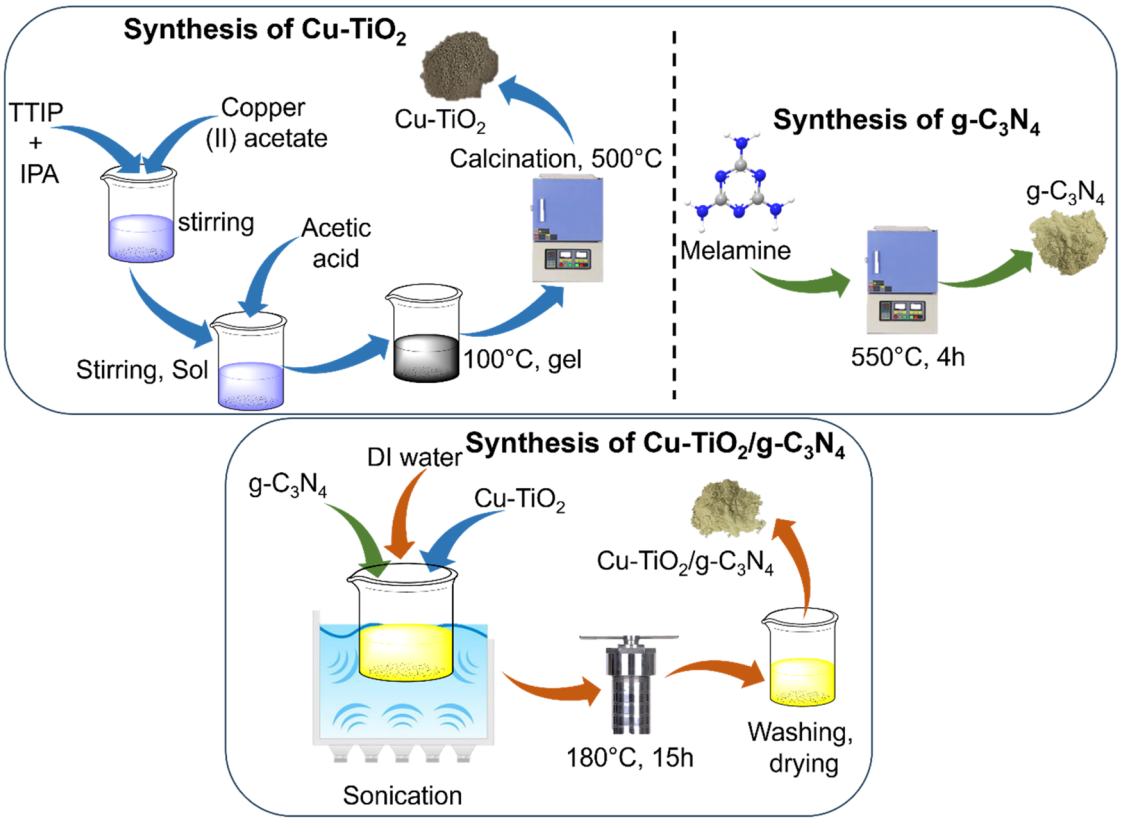

Fig. 1 Schematic illustration of the preparation of Cu-TiO_2/g-C_3N_4 composites.

isopropoxide (TTIP) was mixed with 8.85 mL of isopropyl alcohol under ambient conditions and stirred vigorously for 15 min. To this, 3.0 mL of acetic acid was added and stirring was continued for another 30 min. The mixture was dried at 100 °C for 48 h, and finally, the formed precipitate was calcined at 500 °C for 3 h. For the preparation of Cu-doped TiO_2, an adequate quantity of copper(II) acetate (Cu ratio 3% by using TTIP) was added during the aging process and agitated overnight. Drying and calcination gave the final material.[34]

g-C_3N_4 was prepared by thermal condensation of melamine. In detail, 10 g of melamine was heated to 550 °C for 4 h at a rate of 5 °C min^{-1} in air. The resulting yellow product was ground into powder for further use and denoted as g-C_3N_4.[35]

500 mg of g-C_3N_4, 20 mL of DI water, and 10 mL of ethanol were added to a round bottom flask and sonicated for 30 min. 250 mg (50 wt%) of Cu-TiO_2 were added to the above solution taken in different beakers and sonicated for 15 more min. After sonication, the reaction mixture was stirred for 3 h at room temperature. The resultant mixture was transferred into a 100 mL Teflon-lined autoclave and heated at 180 °C for 15 h. Finally, the autoclave was cooled to room temperature and the resultant solution was centrifuged, washed with water and ethanol several times, and dried at 60 °C overnight.[22]

2.3. Methods of characterization

With an X-ray Ragaku Miniflex I diffractometer (Cu Kα cathode, $\lambda = 0.154056$ nm), X-ray diffraction patterns were acquired and the Scherrer equation was used to estimate the size of the crystallites. Both a transmission electron microscope (TEM) and a scanning electron microscope (SEM) were used to examine the morphology of the nanomaterials. The transmission electron microscope (JEOL JEM 2100) was operated at 200 kV. SEM investigations were conducted using a JEOL 6700F ion beam scanning electron microscope with a 2.5 kV extraction potential and an EDX system. A Thermo Scientific™ ESCALAB Xi + X-ray photoelectron spectrometer was employed to analyze the surface chemistry of the nanomaterials using X-ray photoelectron spectroscopy (XPS). The diffuse reflectance spectra of the prepared particle samples were analyzed using a precision Czerny–Turner optical system in a Shimadzu 1800 UV/visible spectrophotometer. The absorbance of BPA, EB and TC samples was determined using a Shimadzu UV-1990 double-beam UV-visible spectrophotometer.

2.4. Evaluation of photocatalytic performance

The photodegradation of pollutants including bisphenol A (BPA), methylene blue (MB), Congo red (CR) and eriochrome black T under UV-vis light illumination was assessed for the as-prepared photocatalysts. Generally, 50 mg of the photocatalyst was distributed in 100 mL of a solution including BPA (20 ppm) and 10 ppm of MB, CR, and EBT. Prior to photocatalysis, the mixture was agitated in the absence of light for 60 minutes to achieve an adsorption–desorption equilibrium. After 60 min of dark stirring to achieve the equilibrium between adsorption

 © 2025 The Author(s). Published by the Royal Society of Chemistry

Open Access Article. Published on 17 July 2025. Downloaded on 1/22/2026 11:30:53 AM. This article is licensed under a Creative Commons Attribution 3.0 Unported Licence.

and desorption, the suspension was exposed to visible light irradiation using a water circulation cooled 500 W tungsten lamp. The light source was positioned 20 cm away from the suspension. The suspension was sampled at regular irradiation intervals (30 min) for 150 min (BPA, MB and EBT) and 120 min (CR), filtered using a centrifuge machine, and then the concentration of organic pollutants in the solution was analyzed with a UV-vis spectrophotometer at 276 nm, 664 nm, 498 nm, and 489 nm. The degradation efficiencies for organic dyes and BPA were calculated based on eqn (1),

$$\text{Degradation efficiency (\%)} = (C_0 - C_t/C_0) \times 100 \quad (1)$$

where C_t is the concentration at irradiation time t and C_0 is the initial concentration of the pollutant. Using a Shimadzu model TOC-L, the total organic carbon (TOC) concentration was determined.

2.5. Photoelectrochemical measurements

EIS was used in a conventional three-electrode configuration. The as-prepared samples were cast on 1 × 1 cm^2 FTO, which served as the working electrode, and a Ag/AgCl electrode, a platinum electrode, and 0.1 M Na_2SO_4 solution were used as the reference electrode, counter electrode, and electrolyte, respectively. Benzoquinone (BQ), tert-butyl alcohol (TBA), and ammonium oxalate (AO) were used as superoxide radical, hydroxyl radical, and hole scavengers, respectively, in the active species study.

3 Results and discussion

3.1. Structural and morphological studies

The crystal structure of the synthesized nanomaterials was characterized using X-ray diffraction (XRD). The XRD pattern of TiO_2 (Fig. 2a) shows distinct peaks at 27.37°, 35.98°, 41.11°, and 56.63°, corresponding to the (110), (111), (111), and (220) planes of the rutile phase (JCPDS No. 00-021-1276). Additionally, peaks at 25.37°, 36.72°, 37.80°, 38.45°, 48.12°, 53.94°, 55.01°, 62.75°, 68.78°, 70.28°, and 75.02° are indexed to the (101), (103), (004), (002), (105), (211), (204), (115), (220), and other planes of the anatase phase (JCPDS No. 00-021-1272), indicating the coexistence of both rutile and anatase phases.[36] Upon doping with Cu, a slight shift to lower angles in the peak positions of the (101) plane of anatase and the (110) plane of rutile was observed (Fig. 2b), suggesting lattice distortion due to Cu incorporation. This implies successful substitution of Ti^{4+} by Cu^{2+} in the TiO_2 lattice, which is feasible due to the larger ionic radius of Cu^{2+} (0.72 Å) compared to Ti^{4+} (0.60 Å). Notably, no additional peaks corresponding to metallic Cu or copper oxide phases were detected, further indicating that Cu was doped into the TiO_2 lattice rather than forming separate phases.[37]

The XRD pattern of g-C_3N_4 (Fig. 2c) displays two characteristic peaks at 12.87° and 27.44°, which correspond to the (100) and (002) planes, respectively. The composite of Cu-TiO_2 with g-C_3N_4 exhibits diffraction features consistent with those of both Cu-doped TiO_2 and g-C_3N_4, confirming the successful formation of the heterostructure.[38] Although XRD can verify the incorporation of Cu into the crystal lattice, it cannot directly determine its oxidation state. The oxidation state is inferred from the literature and ionic size considerations and should ideally be confirmed by complementary techniques such as XPS.

FT-IR spectra were used to investigate the chemical structure of materials. The broad band located at 500–670 cm^{-1} is attributed to the bending vibrations of the Ti–O–Ti bonds within the TiO_2 lattice (Fig. 2d). The broad band centred at 3100–3600 cm^{-1} is attributed to the intermolecular interaction between the hydroxyl group of the water molecule and the TiO_2 surface (Fig. 2d). The peak at around 1650 cm^{-1} corresponds to the typical bending vibration of the Ti–OH group.[39] The g-C_3N_4 spectra exhibit characteristic stretching vibrations between 1200 and 1700 cm^{-1}, which are ascribed to C–N and C=N heterocycles.[40,41] Broad bands in the range of 3100 to 3300 cm^{-1} and a peak at 802 cm^{-1}, attributed to the N–H stretching vibration of residual NH_2 groups in g-C_3N_4 aromatic rings and the breathing mode of *s*-triazine units, were also detected.[42,43] The primary g-C_3N_4 characteristic peaks were seen in the Cu-TiO_2/g-C_3N_4 spectrum, and the detected band at 500–670 cm^{-1} associated with the Ti–O–Ti and Ti–O bonds can confirm the presence of TiO_2 (Fig. 2d).

EPR is a crucial technique for elucidating the valence state of the dopant and its coordination environment inside the host framework. EPR spectra of Cu-TiO_2 nanoparticles reveal a symmetric structure and indicate octahedral coordination of TiO_2 (Fig. 2e). The *g* value of 1.99 indicates that Cu^{2+} is coordinated in an octahedral arrangement within TiO_2 and has substituted Ti^{4+} at the lattice site. The EPR peak is likewise broad, indicating the presence of dipolar interaction between nearby Cu^{2+} ions, resulting in an increase in peak width.[44] The EPR signal at a *g* value of 2.003 in g-C_3N_4, which was caused by N-defects during exfoliation, indicates an increase in the number of unpaired electrons on C atoms (Fig. 2f).[45]

X-ray photoelectron spectra were used to analyze the surface of the produced catalysts. The survey spectrum of Cu-TiO_2/g-C_3N_4 (Fig. 2g) demonstrates the existence of C, N, Cu, Ti, and O elements. Higher-resolution spectra of synthetic materials were acquired for detailed surface chemical analysis. Three peaks at 284.7, 285.2, and 289.8 eV were seen in the deconvoluted higher resolution C 1s spectrum of Cu-TiO_2/g-C_3N_4 (Fig. 2h), and they are ascribed to sp^2 hybridized C=C, C–O, and O–C=O, respectively.[46] The N 1s spectra (Fig. 2i) reveal three sub-peaks at 398.6, 399.7, and 401.1 eV. These peaks correspond to sp^2 hybridized N in *s*-triazine rings (C–N=C), N–C_3, and N atoms in the heptazine ring.[47] The Cu 2p spectrum of Cu-TiO_2/g-C_3N_4 (Fig. 2j) indicates spin-orbital coupling, with $2p_{3/2}$ and $2p_{1/2}$ appearing at 934.7 and 954.3 eV, respectively, indicating the presence of Cu^{2+}. The Ti 2p spectrum (Fig. 2k) demonstrates spin–orbital coupling, with Ti^{4+} peaks at 457.9 ($2p_{3/2}$) and 463.4 eV ($2p_{1/2}$), respectively. These values are consistent with the Ti^{4+} oxidation state in Ti–O bonds, indicating the presence of TiO_2 rather than metallic Ti. The absence of any shoulder or peak shift toward lower binding energies rules out the presence of metallic Ti (which typically appears at around 457.9 eV for Ti $2p_{3/2}$). Hence, the XPS data confirm that the titanium exists in an oxidized state as part of Ti–O compounds, specifically TiO_2,

Open Access Article. Published on 17 July 2025. Downloaded on 1/22/2026 11:30:53 AM.
This article is licensed under a Creative Commons Attribution 3.0 Unported Licence.

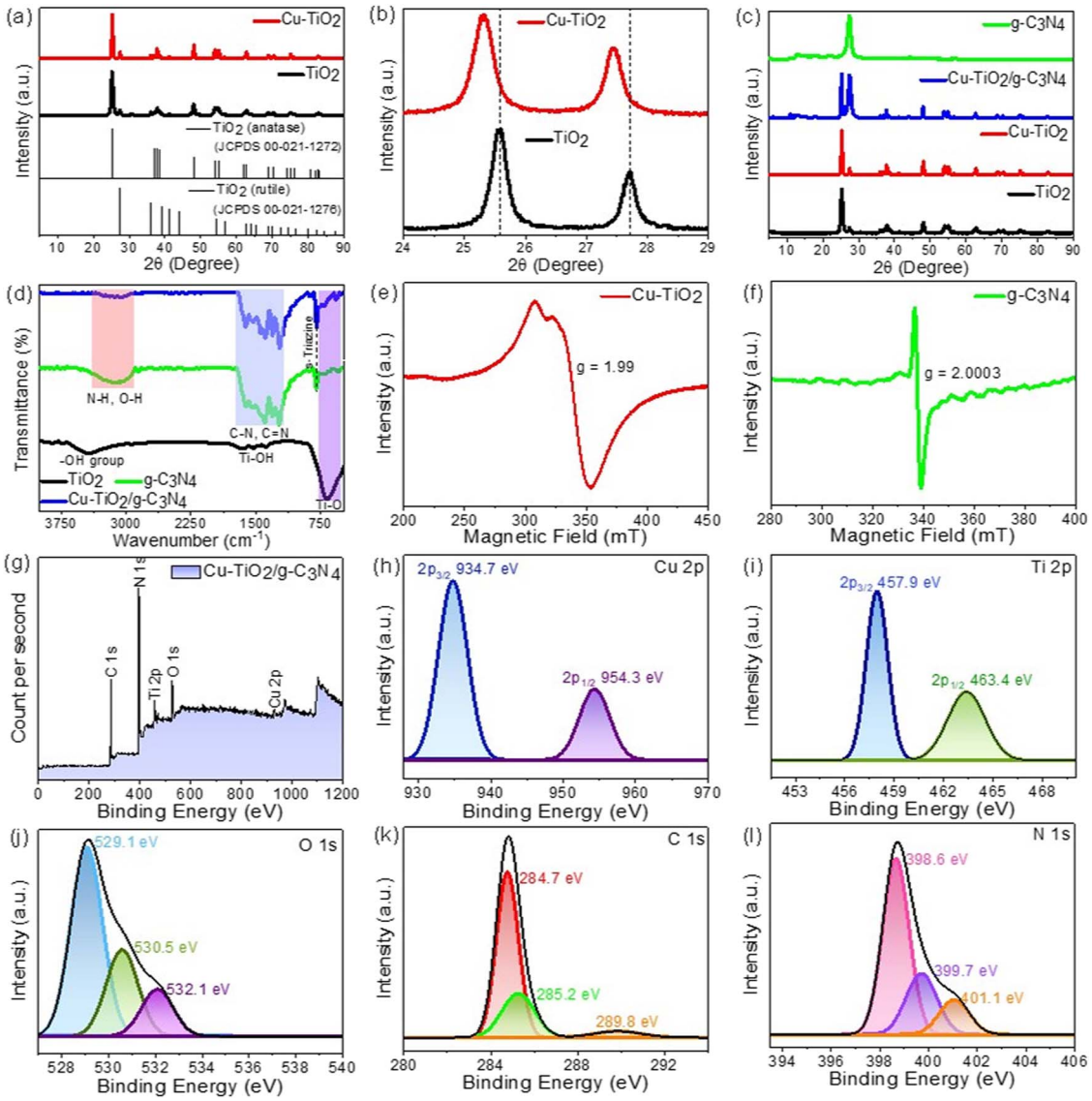

Fig. 2 (a) XRD, (b) enlarged XRD patterns of pristine TiO_2 and Cu-TiO_2, (c) XRD patterns of synthesized materials, (d) FT-IR spectra of the catalysts, EPR spectra of (e) Cu-TiO_2 and (f) g-C_3N_4, (g) XPS survey scan, and high resolution (h) C 1s, (i) N 1s, (j) Cu 2p, (k) Ti 2p, and (l) O 1s XPS spectra.

within the photocatalyst. Three peaks at 529.26, 530.6, and 531.71 eV are identified in the higher resolution O 1s spectra (Fig. 2l), with the third new peak being attributed to the oxygen present in the hydroxyl group or physiosorbed water.[48]

FESEM and TEM examination was used to investigate the morphology of the synthesized pure TiO_2, Cu doped TiO_2, g-C_3N_4 and Cu-TiO_2/g-C_3N_4 photocatalysts (Fig. 3). The pure TiO_2 sample displays irregular, small granular clusters (Fig. 3a and e). In contrast, the Cu-doped TiO_2 sample (Fig. 3b and f) shows a distinct transformation in morphology, characterized by agglomerated spherical particles of uneven size and improved dispersion. These changes in particle shape, size, and distribution suggest that Cu doping significantly alters the microstructure of TiO_2. The incorporation of Cu ions likely occurs near the grain boundaries or on the surface of TiO_2 particles, effectively hindering crystal growth and contributing to the observed morphological differences.[49] Thus, both SEM and TEM effectively support the claim that Cu doping modifies the structural features of TiO_2 at the micro- and nanoscale levels. Fig. 3c illustrates that pure g-C_3N_4 exhibits a distinct irregular layered structure that stacks upon itself. The surface of g-C_3N_4 became rougher than the original g-C_3N_4 as shown in Fig. 3(d and g); this is because loaded Cu-TiO_2 spherical nanoparticles were present. The dispersity of Cu-TiO_2 nanoparticles on the surface of the g-C_3N_4 nanolayer is noticeably better than that of pure TiO_2 nanoparticles. Cu-TiO_2 nanoparticles are uniformly distributed on the g-C_3N_4 sheets, resulting in a rougher and more textured surface. This increased surface area and improved interfacial contact between Cu-TiO_2 and g-C_3N_4 facilitate better light absorption and provide more active sites

 © 2025 The Author(s). Published by the Royal Society of Chemistry

Open Access Article. Published on 17 July 2025. Downloaded on 1/22/2026 11:30:53 AM.
This article is licensed under a Creative Commons Attribution 3.0 Unported Licence.

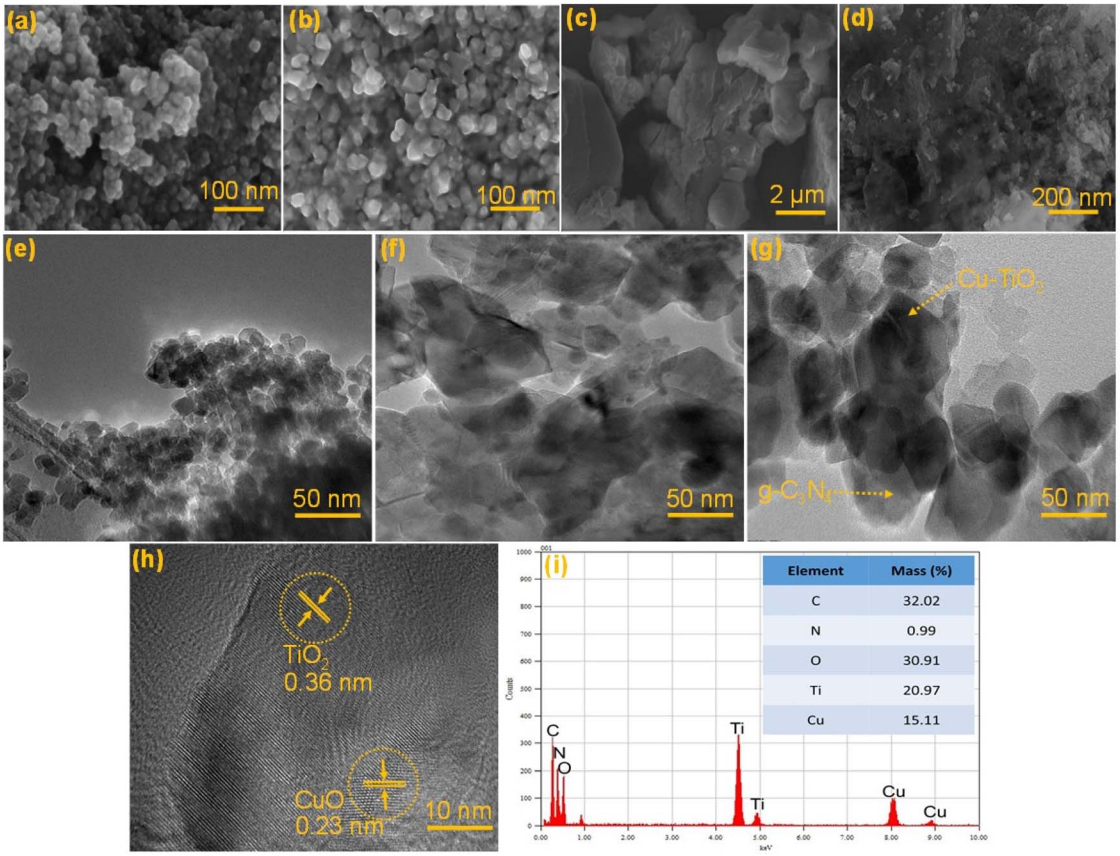

Fig. 3 Scanning electron microscopy (SEM) images of (a) TiO_2, (b) Cu-TiO_2, (c) g-C_3N_4, and (d) Cu-TiO_2/g-C_3N_4 catalysts, transmission electron microscopy (TEM) images of (e) TiO_2, (f) Cu-TiO_2, and (g) Cu-TiO_2/g-C_3N_4, (h) high-resolution transmission electron microscopy (HRTEM) images of Cu-TiO_2/g-C_3N_4, and (i) EDX spectra of Cu-TiO_2/g-C_3N_4 and elemental quantification (inset right).

for photocatalytic reactions, ultimately contributing to enhanced degradation of pollutants. Moreover, the distinct lattice fringe of TiO_2 nanoparticles exhibits a *d*-spacing of 0.36 nm, corresponding to the (101) lattice plane of anatase TiO_2. Fig. 3h shows the high-resolution TEM (HRTEM) image of composites, with a lattice fringe spacing of 0.36 nm corresponding to the (101) crystal plane of TiO_2 and accordingly the (002) crystal plane of g-C_3N_4 revealed that all three phases come into intimate contact with each other and the lattice fringes of the composite structure were strongly defined in their structure. The Cu-TiO_2 nanoparticles loaded on g-C_3N_4 have the same *d*-spacing of 0.36 nm, and the TiO_2 phase is anatase, which is consistent with our prior XRD results.[50] The Cu-TiO_2 nanoparticles in the as-received Cu-TiO_2/g-C_3N_4 nanocomposite grow denser and more uniform, and they exhibit an outstanding heterojunction effect, which is favourable for the transmission of photogenerated electrons and improving photoactivity. Furthermore, energy-dispersive X-ray (EDX) analysis confirmed the presence of all constituent elements, validating the successful synthesis of the Cu-TiO_2/g-C_3N_4 composite, as shown in Fig. 3i.

The optical characteristics of pristine TiO_2, Cu-TiO_2, pristine g-C_3N_4, and Cu-TiO_2/g-C_3N_4 nanocomposite photocatalysts were analyzed to investigate their electronic properties using UV-visible diffuse reflectance spectroscopy. Using UV-vis absorption spectra in the wavelength range of 200–800 nm the photocatalysts were assessed as shown in Fig. 4. TiO_2 shows UV range characteristics, having an absorption edge at 379 nm. The absorption edge of g-C_3N_4 was observed at 449 nm, indicating that it is in the visible range. Conversely, the absorption edge of Cu-TiO_2/g-C_3N_4 is further shifted toward the visible range, indicating that it is in the high visible light absorption range. The optical bandgaps of pristine TiO_2, Cu-TiO_2, pristine g-C_3N_4, and Cu-TiO_2/g-C_3N_4 nanocomposites were calculated using eqn (2):

$$(\alpha h\nu)^n = A(h\nu - E_g) \quad (2)$$

where A is the proportionality constant, α is the extinction coefficient, h is Planck's constant, ν is the frequency of vibration light, E_g is the bandgap, and n is a constant which is 2 or 1/2. The indirect optical bandgap energies were determined by extrapolating the linear portion of the plot $(\alpha h\nu)^{1/2}$ *versus* $h\nu$ (Fig. 4a–d). The calculated E_g values were 3.27, 2.67, 2.78, and 2.77 eV for pristine TiO_2, Cu-TiO_2, pristine g-C_3N_4, and Cu-TiO_2/g-C_3N_4 nanocomposites, respectively. The bandgap of Cu-TiO_2/g-C_3N_4 demonstrates that Cu-doping in TiO_2 can increase the visible light absorption of the Cu-TiO_2/g-C_3N_4 nanocomposite,

Open Access Article. Published on 17 July 2025. Downloaded on 1/22/2026 11:30:53 AM.
This article is licensed under a Creative Commons Attribution 3.0 Unported Licence.

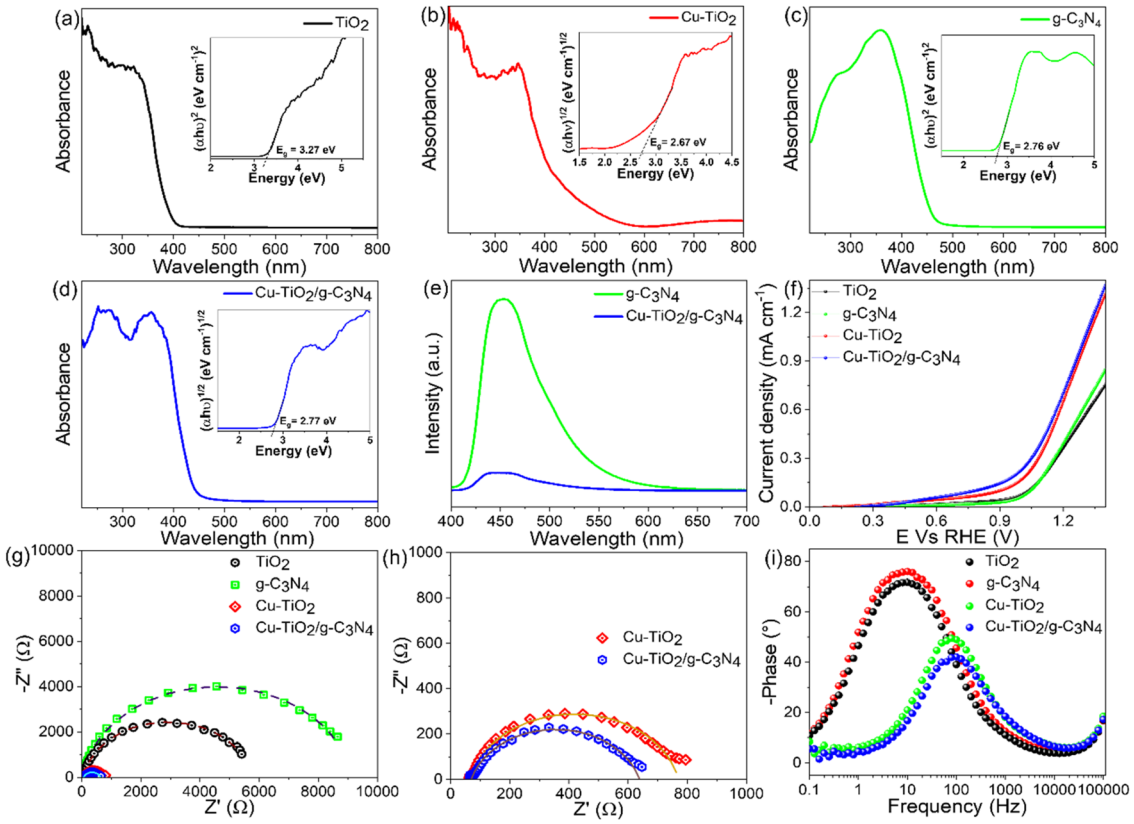

Fig. 4 (a–d) UV-vis diffuse reflectance spectra and Tauc plots of pristine TiO_2, Cu-TiO_2, pristine g-C_3N_4, and Cu-TiO_2/g-C_3N_4 composites, (e) PL spectra of g-C_3N_4 and Cu-TiO_2/g-C_3N_4 composites, (f) polarization curves, (g and h) electrochemical impedance spectra of Cu-TiO_2/g-C_3N_4, and (i) Bode phase plot of photoelectrodes.

resulting in a more significant enhancement in photocatalytic activity.

PL spectra can be used to characterize the separation and migration of photogenerated electron–hole pairs, which is a critical step in photocatalysis. The photoluminescence (PL) spectra arise from the recombination of photogenerated electron–hole pairs, providing insight into their separation efficiency. In general, a high recombination rate of photoexcited electrons and holes results in limited photocatalytic activity. Pristine g-C_3N_4 exhibits the most prominent emission peaks located at around 455 nm (Fig. 4e), which indicate the rapid recombination rate of photoexcited charge carriers and consequently result in reduced photocatalytic activity. When Cu-TiO_2 was loaded with g-C_3N_4, the intensity of emission peaks declined dramatically demonstrating the reduced recombination of electrons and holes. In particular, Cu-TiO_2/g-C_3N_4 with the highest photocatalytic activity even has a much smaller peak intensity than the photocatalyst with g-C_3N_4.

3.2. Photoelectrochemical properties of TiO_2, g-C_3N_4, Cu-TiO_2 and Cu-TiO_2/g-C_3N_4 composites

We studied photoelectrochemical (PEC) behaviour of the fabricated photocatalysts towards the oxygen evolution reaction by fabricating thin films supported on fluorine doped tin oxide as a transparent conducting oxide. The TiO_2 photoanode delivered a photocurrent density (J) 0.4 mA cm^{-2} at 1.23 V_{RHE} meanwhile pristine g-C_3N_4 showed J = 0.42 mA cm^{-2} at 1.23 V_{RHE} (Fig. 4f). Not much difference in activity was observed between TiO_2 and g-C_3N_4 until 1.1 V_{RHE} but above this potential g-C_3N_4 showed slightly higher photocurrent than TiO_2. Doping TiO_2 with Cu led to a significant increase in photocurrent density reaching 0.7 mA cm^{-2} at 1.23 V_{RHE}. However, the composite of Cu-TiO_2/g-C_3N_4 is observed to have higher onset potential and greater photocurrent density even at lower potentials starting from 0.4 V_{RHE} owing to efficient charge generation, separation and transfer at the heterointerface between Cu-TiO_2 and g-C_3N_4. Cu-TiO_2/g-C_3N_4 delivered a photocurrent density of 0.8 mA cm^{-2} at 1.23 V_{RHE} which is significantly higher than that of pristine TiO_2, g-C_3N_4 and Cu-TiO_2 photoanodes. Electrochemical impedance spectroscopy (EIS) is performed to evaluate the charge kinetics of transfer at the bulk and interface. Here, the R_{ct}, R_s, and CPE represent charge transfer resistance, solution resistance, and the constant phase element. The radius of the semicircle represents the obstruction to the flow of charge. The bigger the semicircle radius, the greater the resistance observed by the electrons to flow through the bulk to the surface. A smaller radius depicts easier flow of charge through the bulk to the surface. All the photoanodes showed similar solution resistance owing to being in equilibrium with the electrolyte. On the other hand, charge

© 2025 The Author(s). Published by the Royal Society of Chemistry

Open Access Article. Published on 17 July 2025. Downloaded on 1/22/2026 11:30:53 AM. This article is licensed under a Creative Commons Attribution 3.0 Unported Licence.

transfer resistance (R_{ct}) is observed to be lowest for Cu-TiO_2/g-C_3N_4 (625.5 Ω) as compared to TiO_2 (5700.4 Ω), g-C_3N_4 (9780.3 Ω), and Cu-TiO_2 (760.4 Ω) depicting efficient charge movement from the bulk to the electrode electrolyte in Cu-TiO_2/g-C_3N_4 (Fig. 4(g and h)). Higher charge transfer resistance means obstruction of the flow of charge in the photoanode which might be due to recombination, or destabilization of photoexcited electron/hole pairs due to defects and traps. Bode phase plots were attained from EIS spectroscopy depicting the average electron time period in the circuit. The faster the charge transfer the lower is the electron time period and the higher the average electron time, the slower the electron transfer kinetics in the photoanode making them more prone to recombinations. The average time is inversely proportional to the frequency maxima of the photoanode in the Bode phase plot. Here in our study, we found that Cu-TiO_2/g-C_3N_4 showed the lowest phase difference and highest time (maxima at high frequency) compared to TiO_2, g-C_3N_4, and Cu-TiO_2 (Fig. 4i).

3.3. Photocatalytic study

3.3.1. Effect of synthesized catalysts on the photocatalytic removal and mineralization of bisphenol A, methylene blue, Congo red and eriochrome black T. The degradation of persistent organic pollutants, such as the endocrine disruptor bisphenol A (BPA) and dyestuffs of methylene blue (MB), Congo red (CR), and eriochrome black T (EBT) under visible light, was conducted to compare the photocatalytic activities of TiO_2, Cu-TiO_2, g-C_3N_4, and Cu-TiO_2/g-C_3N_4 samples. To better understand the dynamic degradation process of BPA, MB, CR and EBT on different photocatalysts, the first-order kinetic model with equation $-\ln(C_t/C_0) = kt$ is used to describe the experimental data, where C_t (ppm) is the residual concentration at time t (min) and C_0 is the concentration at $t = 0$. The degradation rate constants (k) of pollutants are described in Table 1 and Fig. 5.

The rate constants and time-resolved degradation profiles of BPA, MB, CR, and EBT under visible light irradiation with photocatalysts are shown in Fig. 5a–d. The incorporation of TiO_2 results in the elimination efficiencies for BPA, MB, CR, and EBT being 35% (150 min), 78% (150 min), 46% (120 min), and 30% (150 min), respectively. The corresponding removal percents in the Cu-TiO_2/visible irradiation system are 74% (BPA), 92% (MB), 78% (CR), and 80% (EBT). The BPA, MB, CR, and EBT degradation efficiencies are 40%, 90%, 54%, and 47% for g-C_3N_4/visible, respectively. The photocatalytic efficiencies of Cu-TiO_2/g-C_3N_4 in the degradation of BPA, MB, CR, and EBT are 99%, 99%, 86%, and 92% respectively. Clearly, Cu-TiO_2, g-C_3N_4, and Cu-TiO_2/g-C_3N_4 catalysts have better visible light photocatalytic degradation efficiencies towards BPA, MB, CR and EBT elimination than TiO_2 (Fig. S1 and S2†). The total organic carbon removal efficiency for BPA, MB, CR, and EBT is 40%, 45%, 35% and 29%, respectively, implying that TOC mineralization of the typical endocrine disruptor and dyestuffs over the photocatalysts of Cu-TiO_2/g-C_3N_4 is favourable under visible light after irradiation for 150 min, 150 min, 120 min and 150 min (Fig. 6d). The improved photocatalytic performance is primarily due to enhanced visible light absorption and the effective transfer and separation of photoinduced electrons and holes, which depend on the well-established interface between Cu-TiO_2 and g-C_3N_4. However, doping Cu into TiO_2 resulted in a shift in the valence band position of TiO_2, and Cu-TiO_2 nanoparticles agglomerated on the surface of g-C_3N_4 stacked layers, thereby forming a heterojunction structure and enhancing photocatalytic activity. Table 2 shows the comparison of the photocatalytic activity of the various developed heterojunctions with those of the previously reported UV-vis light photocatalysts for the photodegradation of BPA.

Table 1 Pseudo-first-order rate constants (min^{-1}) for BPA, MB, CR, and EBT degradation under UV-vis light irradiation

	k (min^{-1})			
Photocatalyst	BPA	MB	CR	EBT
TiO_2	0.0018	0.0063	0.0034	0.0015
g-C_3N_4	0.0022	0.0097	0.0041	0.0026
Cu-TiO_2	0.0056	0.0122	0.0085	0.0069
Cu-TiO_2/g-C_3N_4	00.0195	0.0186	0.0109	0.0098

3.3.2. Effect of operational parameters on photocatalytic properties

3.3.2.1 Effect of the initial concentration of BPA. With 40 mg of Cu-TiO_2/g-C_3N_4, the amount of BPA was changed from 20 to 40 ppm. At 20 ppm of BPA, the rate of photodegradation was faster, with a rate constant of 0.0195 min^{-1} (Fig. 6a). The photodegradation rate was reported to be 98% at this concentration (20 ppm). The reduction in photodegradation efficiency to 40% at a BPA concentration of 40 ppm was ascribed to the formation of BPA on the Cu-TiO_2/g-C_3N_4 surface, which blocks direct light irradiation to the catalyst surface.

3.3.2.2 Effect of the catalyst concentration. The concentration of the catalyst in photocatalytic processes significantly affects the breakdown of BPA. Different catalyst concentrations, ranging from 30 mg to 50 mg, were used in the experiments. The efficiency of BPA degradation increases with an increasing catalyst concentration up to 40 mg, after which it slightly decreases with additional catalyst concentrations as demonstrated in Fig. 6b. The decomposition of BPA is accelerated by increases in the quantity of active sites and absorbed photons on the photocatalyst surface. However the particles aggregate, the specific surface areas decrease, and ultimately the photocatalytic activity is lowered if the catalyst concentration is higher than the ideal amount.

3.3.2.3 Effect of pH. The initial pH is a crucial component in the photocatalytic reaction. The effect of starting pH on BPA photodegradation was demonstrated using single factor studies, with observations illustrated in Fig. 6c. At pH 3 the BPA elimination rate attained the highest degree of degradation efficiency. In an acidic medium, BPA molecules become protonated, which alters their electronic structure. The phenol groups in BPA can accept H^+ ions, making the molecule more reactive to photochemical processes. The degradation rate constants (k) of BPA concerning photocatalytic factors, including the BPA concentration, catalyst concentration (Cu-

Open Access Article. Published on 17 July 2025. Downloaded on 1/22/2026 11:30:53 AM.
This article is licensed under a Creative Commons Attribution 3.0 Unported Licence.

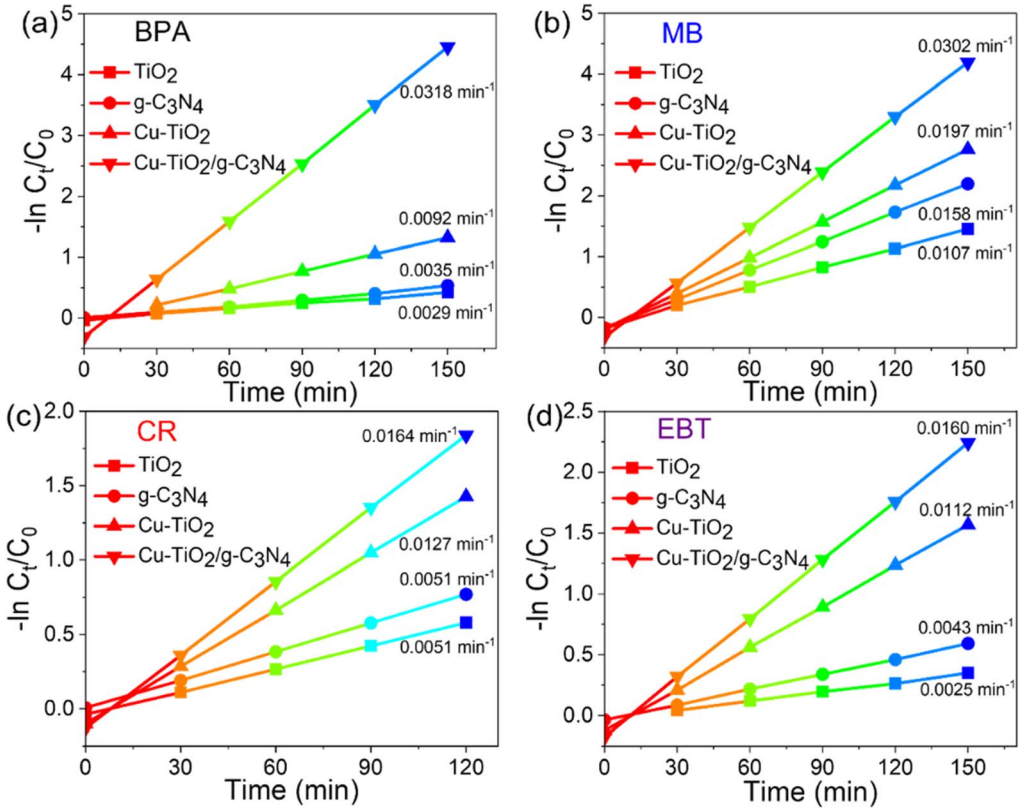

Fig. 5 Plots of $-\ln(C/C_0)$ *vs.* time for the photodegradation of (a) bisphenol A, (b) methylene blue, (c) Congo red and (d) eriochrome black T under visible light irradiation with various catalysts. Experimental conditions: pollutants (BPA, MB, CR and EBT) = 50 mL (10 ppm), catalysts = 50 mg.

TiO_2/g-C_3N_4), and pH impact, can be derived from the slope of the fitting line in the plot of $-\ln(C_t/C_0)$ *versus* time (t). The plots of C_t/C_0 *versus* time and the degradation efficiencies illustrating the effects of operational parameters such as initial concentration, catalyst dosage, and pH on the photocatalytic performance are presented in Fig. S3 and S4.†

3.3.3. Reusability of the most efficient photocatalyst Cu-TiO_2/g-C_3N_4. In order to study the stability and reusability, the collected Cu-TiO_2/g-C_3N_4 sample was reused for degradation of BPA under visible light irradiation. The recycled Cu-TiO_2/g-C_3N_4 retains satisfactory reusing performance in which the BPA degradation efficiencies after five continuous runs are 90% (Fig. 7a). The little decline compared with the primary cycle in degradation activities suggests that Cu-TiO_2/g-C_3N_4 has considerable reusability for visible light driven photocatalysis. This can be confirmed by the information in XRD patterns (Fig. 7b) and XPS survey scan (Fig. 7c) of Cu-TiO_2/g-C_3N_4 before and after the 5th BPA degradation cycle. As can be seen, the recycled sample shows extremely similar diffraction peaks to the fresh one, indicating that the phase and structure of Cu-TiO_2/g-C_3N_4 have no obvious change after the photocatalytic reaction. Further investigation is carried out by using XPS to determine the chemical constituents of the recycled Cu-TiO_2/g-C_3N_4 sample. From the figure of XPS spectra survey scan, it can be found that the recycled Cu-TiO_2/g-C_3N_4 contains Cu 2p, Ti 2p, O 1s, C 1s and N 1s as well as the fresh material. As these results show, Cu-TiO_2/g-C_3N_4 can be used as an efficient photocatalyst for application in wastewater treatment.

3.4. Photocatalytic mechanism

In order to explore the intrinsic reaction mechanism involving different reactive species during the photocatalytic degradation process, typical radical scavenging experiments for BPA degradation over Cu-TiO_2/g-C_3N_4 are performed. *p*-benzoquinone, tert-butyl alcohol and ammonium oxalate are chosen as the quenchers of superoxide radicals ($O_2^{-\bullet}$), photo-induced holes (h^+) and hydroxyl radicals ($OH^\bullet$), respectively. As presented in Fig. 7d, the BPA photodegradation efficiency of Cu-TiO_2/g-C_3N_4 under visible light drastically decreased by 32% after addition of ammonium oxalate, which suggests that photo-induced holes play a key role in the degradation of BPA. In the presence of tert-butyl alcohol, the removal ratio of BPA is obviously restricted, in which 74% BPA degradation efficiency is perceived with a loss of photodegradation percent indicating that the photo-generated $OH^\bullet$ is also the main factor affecting BPA degradation under visible light irradiation. In addition, it can be found that the existence of *p*-benzoquinone also has a noticeable impact on BPA degradation (83%), which implies that the $O_2^{-\bullet}$ species is also involved in the PBA degradation process by Cu-TiO_2/g-C_3N_4. Therefore, the results demonstrate that the three reactive species are responsible for BPA

© 2025 The Author(s). Published by the Royal Society of Chemistry

Open Access Article. Published on 17 July 2025. Downloaded on 1/22/2026 11:30:53 AM.
This article is licensed under a Creative Commons Attribution 3.0 Unported Licence.

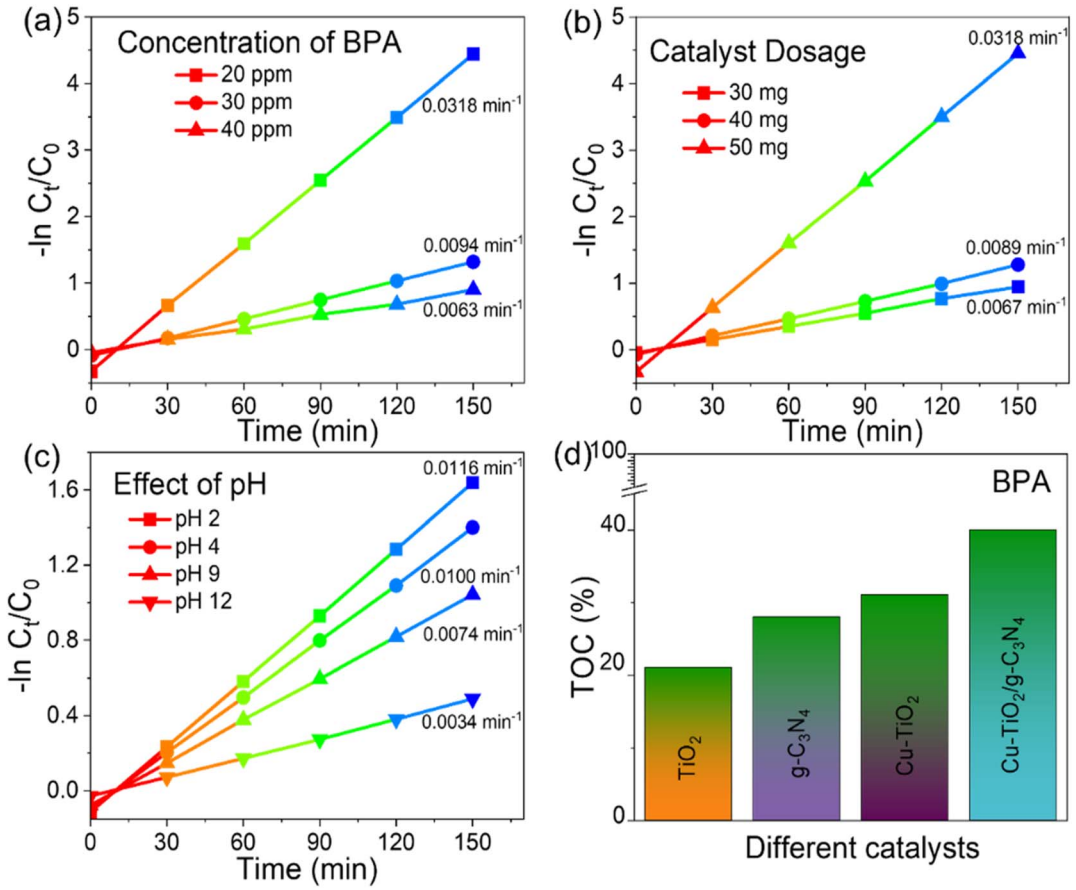

Fig. 6 Plots of $-\ln(C_t/C_0)$ *vs.* time for the photodegradation of BPA with respect to (a) concentration effect of BPA, (b) catalyst dosage of Cu-TiO_2/g-C_3N_4, and (c) effect of pH, and (d) TOC analysis of BPA photodegradation.

degradation and the contribution order of these reactive species is $h^+ > OH^\bullet > O_2^{-\bullet}$. Photocatalytic degradation (concentration *vs.* time) and $-\ln(C_t/C_0)$ *vs.* time plots for the impact of quenchers over Cu-TiO_2/g-C_3N_4 for BPA degradation are described in Fig. S5.† To improve the photocatalytic activity of bare Cu-TiO_2 and g-C_3N_4, Cu-TiO_2/g-C_3N_4 heterostructures were fabricated to minimize the recombination of photogenerated electron–hole pairs and facilitate effective charge separation. As mentioned earlier, the fast e^- and h^+ recombination is the main drawback of using a single photocatalyst. Furthermore, the h^+ and e^- produced by g-C_3N_4 and Cu-TiO_2, respectively, are insufficient for reacting with H_2O and O_2. The redox potential of h^+ and e^- was preserved by Cu-TiO_2/g-C_3N_4, which also inhibited their quick recombination. Hence, compared to bare Cu-TiO_2 or g-C_3N_4, Cu-TiO_2/g-C_3N_4 showed substantially superior photocatalytic activity for BPA degradation. The inadequate photocatalytic performance of g-C_3N_4 is ascribed to the recombination phenomena of photogenerated electron (e^-)–

Table 2 Comparison of the photocatalytic activity of the various developed heterojunctions with those of the previously reported UV-vis light photocatalysts for the photodegradation of BPA

Photocatalyst	Pollutant	Time (min)	Light source	Photodegradation (%)	Ref.
$CuBi_2O_4$/Zn-Al LDH	BPA	240	Visible	84	51
TiO_2/WS_2		120	Visible	85	52
Ag/Bi_3O_4Br		90	Sun light	94	53
$In_2S_3/Zn_3In_2S_6$		120	Visible	95	54
GO@BiOI/Bi_2WO_6		360	UV-vis	81	55
Bi_3O_4Br/Ti_3C_2		60	Visible	91	56
Ag-TiO_2		120	UV	96	57
C_3N_4-Zn/Bi_2WO_6		120	Visible	93	58
Cu-TiO_2/g-C_3N_4		180	Visible	99	This work

© 2025 The Author(s). Published by the Royal Society of Chemistry

Open Access Article. Published on 17 July 2025. Downloaded on 1/22/2026 11:30:53 AM.
This article is licensed under a Creative Commons Attribution 3.0 Unported Licence.

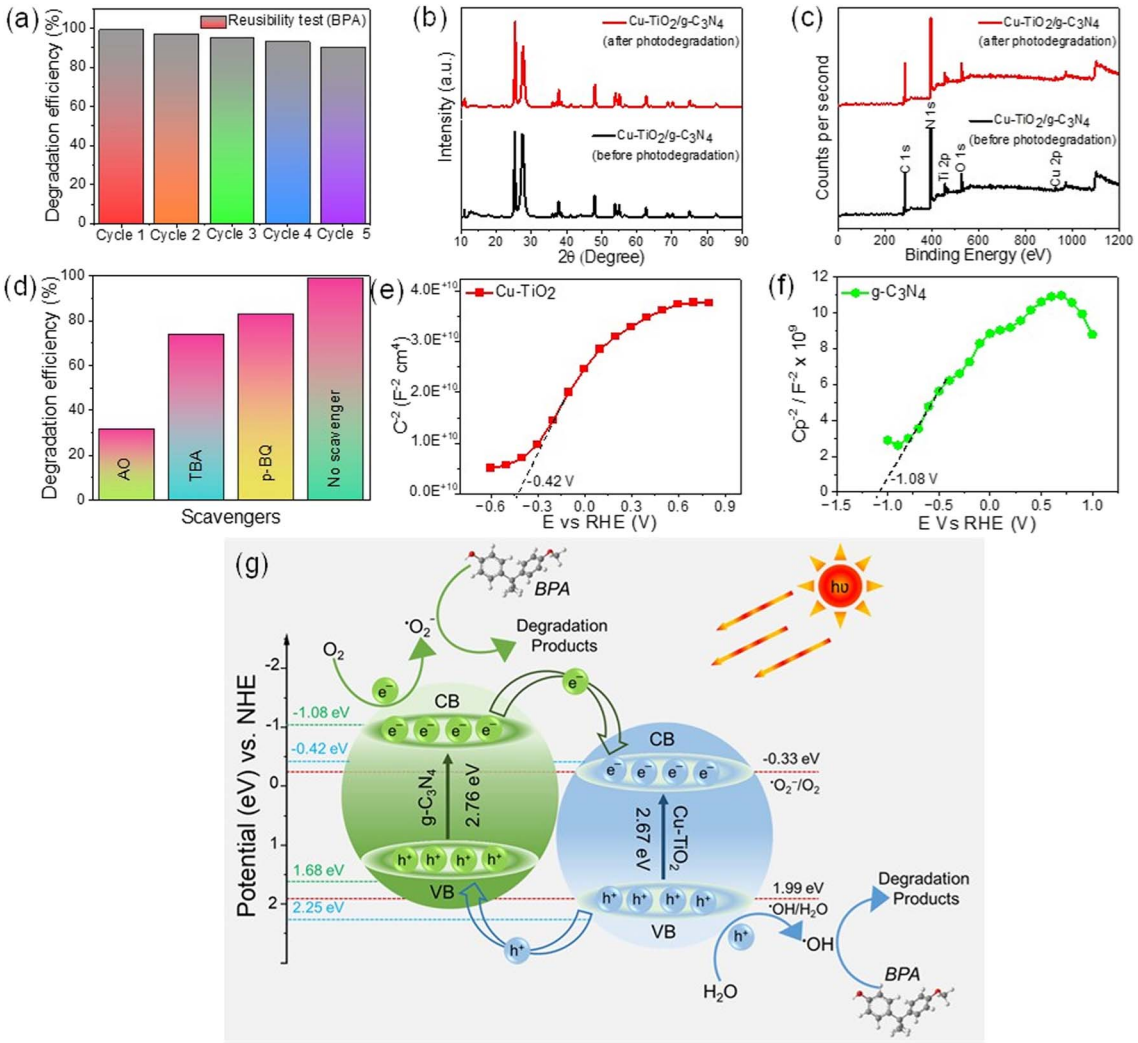

Fig. 7 (a) Degradation efficiency of the Cu-TiO_2/g-C_3N_4 photocatalyst in the reusability test under visible light irradiation, (b) XRD spectra and (c) XPS spectra after five cycles, (d) impact of quenchers over Cu-TiO_2/g-C_3N_4, Mott–Schottky (M–S) plots of (e) Cu-TiO_2 and (f) g-C_3N_4 and (g) possible reaction mechanism for BPA photodegradation.

hole (h^+) pairs. Therefore, the most effective method to improve photocatalytic activity is by creating composites or heterojunctions of g-C_3N_4 with various metal oxides. The energy band locations of the valence band (VB) maxima and conduction band (CB) minima are used to assess the photocatalytic degradation mechanism of Cu-TiO_2/g-C_3N_4 heterostructures. The maximum position of the valence band (VB) for g-C_3N_4 is about 1.68 eV, and the minimum position of the conduction band (CB) is around −1.08 eV. For Cu-TiO_2, the VB is at 2.25 eV and the CB is at −0.42 eV according to Mott–Schottky (M–S) plots (Fig. 7(e and f)). The Cu-TiO_2/g-C_3N_4 composite starts to produce photo-induced electrons and holes when exposed to visible light. Electrons that are stimulated using light go from the valence band (VB) into the conduction band (CB). Electrons from the CB of g-C_3N_4 migrate to the CB of Cu-TiO_2, while holes migrate in the opposite direction, specifically from the VB of Cu-TiO_2 to the VB of g-C_3N_4. Consequently, the effective separation of photoinduced electron–hole pairs is facilitated by the heterojunction that is formed between semiconductors with appropriate band potentials (Fig. 7g). The photocatalytic activity is improved by the synergistic effect of Cu-TiO_2 and g-C_3N_4, which promotes charge separation. The amalgamation of Cu-TiO_2 and g-C_3N_4 facilitates charge separation and enhances photocatalytic activity. The surface-migrated electrons react with dissolved oxygen to generate superoxide radical anions ($O_2^{\bullet-}$), while holes in the valence band react with water to produce highly reactive hydroxyl radicals ($^{\bullet}OH$), both of which oxidize deleterious organic compounds.

4 Conclusions

We were able to decrease the band gap and increase the visible light response by successfully incorporating Cu into a TiO_2 lattice. A Cu-TiO_2/g-C_3N_4 heterojunction photocatalyst was also effectively created by integrating Cu-TiO_2 with g-C_3N_4. A highly visible light active photocatalyst heterojunction of g-C_3N_4 layer

© 2025 The Author(s). Published by the Royal Society of Chemistry

Open Access Article. Published on 17 July 2025. Downloaded on 1/22/2026 11:30:53 AM. This article is licensed under a Creative Commons Attribution 3.0 Unported Licence.

anchored Cu-TiO_2 was synthesized by the hydrothermal method for endocrine disruptor and cationic and anionic dye stuff degradation. The Cu-TiO_2/g-C_3N_4 photocatalyst promoted the absorption of visible light and separation of photogenerated charges resulting in the enhancement of photocatalytic activity. Among the tested photocatalysts, Cu-TiO_2/g-C_3N_4 shows the maximum enhanced photocatalytic performance compared to TiO_2, Cu-TiO_2 and g-C_3N_4 towards BPA, MB, CR and EBT degradation under visible light irradiation. The degradation process of BPA is mainly caused by h^+ and $OH^\bullet$ free radicals with high oxidation activity generated on the CB of g-C_3N_4 and VB of Cu-TiO_2, respectively, attributing to energy band matching. According to the considerable reusability and stability certified by recycling tests, the heterojunction photocatalyst based on Cu-TiO_2/g-C_3N_4 has great potential in pollution control and remediation of water environments.

Data availability

The data that support the findings of this study are available from the corresponding author upon reasonable request.

Author contributions

Phyu Phyu Cho: writing – original draft, visualization, methodology, investigation, formal analysis, data curation, conceptualization, writing – review & editing. Phyu Phyu Mon: methodology, formal analysis, investigation. Mohit Kumar: investigation, methodology, writing – review & editing. Saiyam Dobhal: investigation, methodology. Challapalli Subrahmanyam: conceptualization, writing – review & editing, visualization, validation, supervision, project administration, funding acquisition.

Conflicts of interest

There are no conflicts to declare.

Acknowledgements

Phyu Phyu Cho and Phyu Phyu Mon are thankful to the DIA-Doctoral Fellowship in India for ASEAN for financial assistance and the Indian Institute of Technology Hyderabad for the facility. Mohit Kumar would like to thank the CSIR-India for a senior research fellowship and SUPRA fellowship from the Swinburne University of Technology, Australia.

References

1 K. Wang, J. Li and G. Zhang, *ACS Appl. Mater. Interfaces*, 2019, **11**, 27686–27696.
2 G. K. Pradhan, D. K. Padhi and K. M. Parida, *ACS Appl. Mater. Interfaces*, 2013, **5**, 9101–9110.
3 Md. S. A. Sher Shah, A. R. Park, K. Zhang, J. H. Park and P. J. Yoo, *ACS Appl. Mater. Interfaces*, 2012, **4**, 3893–3901.
4 Y. Li, Z. Tang, J. Zhang and Z. Zhang, *Appl. Catal., A*, 2016, **522**, 90–100.
5 M. Ahmad, E. Ahmed, Z. L. Hong, J. F. Xu, N. R. Khalid, A. Elhissi and W. Ahmed, *Appl. Surf. Sci.*, 2013, **274**, 273–281.
6 K. Jahanara and S. Farhadi, *RSC Adv.*, 2019, **9**, 15615–15628.
7 W. Li and L. Xu, *Acta Chim. Sin.*, 2019, **77**, 705.
8 M. Kumar, P. P. Cho, R. K. Sethi, V. Biju and C. Subrahmanyam, *J. Photochem. Photobiol., C*, 2025, **64**, 100710.
9 C.-D. Dong, C.-W. Chen and C.-M. Hung, *Bioresour. Technol.*, 2017, **245**, 188–195.
10 L. S. Yoong, F. K. Chong and B. K. Dutta, *Energy*, 2009, **34**, 1652–1661.
11 T. Woo Kim, H.-W. Ha, M.-J. Paek, S.-H. Hyun, J.-H. Choy and S.-J. Hwang, *J. Mater. Chem.*, 2010, **20**, 3238–3245.
12 F. Andish-Lifshagerd, A. Habibi-Yangjeh, M. Habibi and Y. Akinay, *J. Photochem. Photobiol., A*, 2024, **448**, 115351.
13 M. Habibi, A. Habibi-Yangjeh, Y. Akinay and A. Khataee, *Chemosphere*, 2023, **340**, 139828.
14 T. Kobkeatthawin, S. Chaveanghong, J. Trakulmututa, T. Amornsakchai, P. Kajitvichyanukul and S. M. Smith, *Nanomaterials*, 2022, **12**, 2852.
15 X. Geng, L. Wang, L. Zhang, H. Wang, Y. Peng and Z. Bian, *Chem. Eng. J.*, 2021, **420**, 129722.
16 V. V. Pham, T. K. Truong, L. V. Hai, H. P. P. La, H. T. Nguyen, V. Q. Lam, H. D. Tong, T. Q. Nguyen, A. Sabbah, K.-H. Chen, S.-J. You and T. M. Cao, *ACS Appl. Nano Mater.*, 2022, **5**, 4506–4514.
17 K. N. Van, H. T. Huu, V. N. Nguyen Thi, T. L. Le Thi, D. H. Truong, T. T. Truong, N. N. Dao, V. Vo, D. L. Tran and Y. Vasseghian, *Chemosphere*, 2022, **289**, 133120.
18 M. Preeyanghaa, V. Vinesh and B. Neppolian, *Chemosphere*, 2022, **287**, 132380.
19 J. Yang, Z. Liu, Y. Wang and X. Tang, *New J. Chem.*, 2020, **44**, 9725–9735.
20 Z. Zhu, R. Kumar, L. Luo, S. Varjani, P. Huo, J. Woon-Chung Wong and J. Zhao, *Catal. Sci. Technol.*, 2022, **12**, 6384–6397.
21 X. Yu, Z. Liu, Y. Wang, H. Luo and X. Tang, *New J. Chem.*, 2020, **44**, 15908–15918.
22 H. Liyanaarachchi, C. Thambiliyagodage, C. Liyanaarachchi and U. Samarakoon, *Arabian J. Chem.*, 2023, **16**, 104749.
23 Y. Huang, X. Xu, G. Fan, X. Zhu, L. Zhu and X. Chen, *Colloids Surf., A*, 2024, **694**, 134170.
24 M. A. F. Md Fauzi, M. H. Razali, M. U. Osman and B. M. Azam, *Adv. Mater. Process. Technol.*, 2022, **8**, 4395–4415.
25 M. Li, B. Dong, Z. Chang, H. Dang, S. Ma and W. Li, *Waste Biomass Valorization*, 2023, **14**, 687–701.
26 M. H. Hazaraimi, P. S. Goh, L. Y. Wang, W. J. Lau, M. N. Subramaniam, A. F. Ismail, N. Hashim, N. D. Kerisnan, N. K. E. M. Yahaya and R. B. R. Mamat, *Arabian J. Sci. Eng.*, 2025, **50**, 4367–4381.
27 A. Miri, Y. Shih and W.-L. Chen, *Chemosphere*, 2024, **362**, 142658.
28 L. S. Alqarni, M. D. Alghamdi, H. Alhussain, N. Y. Elamin, K. K. Taha and A. Modwi, *J. Mater. Sci.: Mater. Electron.*, 2024, **35**, 239.
29 H. Zhang, G. Zhang, H. Zhang, Q. Tang, Y. Xiao, Y. Wang and J. Cao, *Appl. Surf. Sci.*, 2021, **567**, 150833.

© 2025 The Author(s). Published by the Royal Society of Chemistry

Open Access Article. Published on 17 July 2025. Downloaded on 1/22/2026 11:30:53 AM. This article is licensed under a Creative Commons Attribution 3.0 Unported Licence.

30 P. Eskandari, E. Amarloo, H. Zangeneh, M. Rezakazemi and T. M. Aminabhavi, *Chemosphere*, 2023, **337**, 139282.
31 E. D. Mohamed Isa, R. Rasit Ali, N. W. Che Jusoh, Y. Nagao, K. Aoki, S. Nishimura, Z. I. Ahmad Tarmizi and S. H. Mohd Taib, *Colloids Surf., A*, 2024, **694**, 134066.
32 A. S. Karthik, S. Senthil, D. Tamilselvi, R. Rathinam and V. Jeevanantham, *J. Indian Chem. Soc.*, 2024, **101**, 101424.
33 P. Hemmati-Eslamlu, A. Habibi-Yangjeh, Y. Akinay and T. Cetin, *J. Photochem. Photobiol., A*, 2023, **443**, 114862.
34 P. Phyu Cho, P. Phyu Mon, K. V. Ashok Kumar, M. Kumar, P. Ghosal, N. Lingaiah, G. Madras and Ch. Subrahmanyam, *Inorg. Chem. Commun.*, 2023, **156**, 111147.
35 P. P. Cho, P. P. Mon, D. Vidyasagar, G. Madras and Ch. Subrahmanyam, *New J. Chem.*, 2023, **47**, 17775–17782.
36 D. O. Adekoya, M. Tahir and N. A. S. Amin, *J. CO_2 Util.*, 2017, **18**, 261–274.
37 J.-Y. Chen, J.-K. Yan and G.-Y. Gan, *J. Spectrosc.*, 2019, **2019**, e6470601.
38 A. M. Hamza and H. A. Alshamsi, *Sci. Rep.*, 2024, **14**, 23596.
39 S. S. Al-Taweel, H. R. Saud, A. A. H. Kadhum and M. S. Takriff, *Results Phys.*, 2019, **13**, 102296.
40 X. Chen, D.-H. Kuo and D. Lu, *RSC Adv.*, 2016, **6**, 66814–66821.
41 V.-H. Nguyen, M. Mousavi, J. B. Ghasemi, S. A. Delbari, Q. V. Le, M. Shahedi Asl, M. Shokouhimehr, M. Mohammadi, Y. Azizian-Kalandaragh and A. Sabahi Namini, *J. Taiwan Inst. Chem. Eng.*, 2020, **115**, 279–292.
42 S. Chen, X. Li, W. Zhou, S. Zhang and Y. Fang, *Appl. Surf. Sci.*, 2019, **466**, 254–261.
43 Y. Yang, J. Chen, Z. Mao, N. An, D. Wang and B. D. Fahlman, *RSC Adv.*, 2017, **7**, 2333–2341.
44 H. Zhang, M. Wang and F. Xu, *Micro Nano Lett.*, 2020, **15**, 535–539.
45 Q. Liu, T. Chen, Y. Guo, Z. Zhang and X. Fang, *Appl. Catal., B*, 2016, **193**, 248–258.
46 S. Gong, Z. Jiang, S. Zhu, J. Fan, Q. Xu and Y. Min, *J. Nanopart. Res.*, 2018, **20**, 310.
47 Y. Zou, B. Yang, Y. Liu, Y. Ren, J. Ma, X. Zhou, X. Cheng and Y. Deng, *Adv. Funct. Mater.*, 2018, **28**, 1806214.
48 Y.-Q. Zhang, N. Xu, Y. Liu, X. Zhang, W.-Z. Li, H.-T. Zhao and J. Luan, *RSC Adv.*, 2022, **12**, 9363–9372.
49 T. Feng, G. Feng, L. Yan and J. H. Pan, *Int. J. Photoenergy*, 2014, **2014**, 1–14.
50 X. Chen, X. Zhang, H. Wang, H. Guo and W. Cui, *J. Mater. Sci.*, 2024, **59**, 17846–17859.
51 T. Ma, Y. Mao, C. Liu, M. Sun, Z. Li, M. Chen, R. Zheng, S. Dai, X. Guo and T. Zhao, *J. Alloys Compd.*, 2023, **941**, 169032.
52 N. J. Ismail, M. H. D. Othman, H. S. Zakria, S. Borhamdin, M. S. Moslan, M. H. Puteh, J. Jaafar, N. Hashim, N. D. A. / P. Kerisnan and N. K. E. M. Yahaya, *J. Mater. Sci.*, 2024, **59**, 12361–12383.
53 X. Jiang, X. He, H. Huang, Y. Li, J. Yang, J. Mei and S. Cui, *J. Alloys Compd.*, 2023, **963**, 171221.
54 L. Yang, A. Li, T. Dang, Y. Wang, L. Liang, J. Tang, Y. Cui and Z. Zhang, *Appl. Surf. Sci.*, 2023, **612**, 155848.
55 Z. Mengting, T. A. Kurniawan, Y. Yanping, R. Avtar and M. H. D. Othman, *Mater. Sci. Eng. C*, 2020, **108**, 110420.
56 Y. Wang, F. Xie, R. Li, Z. Yu, X. Jian, X. Gao, H. Li, X. Zhang, J. Liu, X. Zhang, Y. Wang, C. Fan, X. Yue and A. Zhou, *Sep. Purif. Technol.*, 2023, **318**, 124001.
57 R. Hidayat, G. Fadillah, S.-I. Ohira, F. I. Fajarwati, D. A. Setyorini and A. Saputra, *Mater. Today Sustain.*, 2024, **26**, 100752.
58 X. Ruan and Y. Hu, *Chemosphere*, 2020, **246**, 125782.

© 2025 The Author(s). Published by the Royal Society of Chemistry